Horizontal Planar Angular Light Scattering (HPALS) characterization of soot produced in a laminar axisymmetric coflow ethylene diffusion flame

Jerôme Yon, José Morán, Florian Lespinasse, Felipe Escudero, G. Godard, Marek Mazur, Fengshan Liu, Andrés Fuentes

Version of Record: https://www.sciencedirect.com/science/article/pii/S0010218021002820
Manuscript_e35bf9a06866bb91037c594dd207b6a9

Horizontal Planar Angular Light Scattering (HPALS) characterization of soot produced in a Laminar Axisymmetric Coflow Ethylene Diffusion Flame

Jérôme Yon[a,*], José Morán[a], Florian Lespinasse[a], Felipe Escudero[c], Gilles Godard[a], Marek Mazur[a], Fengshan Liu[b], Andrés Fuentes[c]

[a]*Normandie Univ, UNIROUEN, INSA Rouen, CNRS, CORIA, 76000 Rouen, France.*
[b]*Metrology Research Centre, National Research Council of Canada, Ottawa, Ontario, Canada.*
[c]*Departamento de Industrias, Universidad Técnica Federico Santa María, Av. España 1680, Casilla 110-V, Valparaíso, Chile.*

Abstract

In-flame optical characterization of soot is of vital importance to understand soot formation mechanisms as well as to develop and validate accurate soot models. The present work introduces an unconventional methodology adapted to laminar axisymmetric flames that avoids the issue of variable measurement volume with varying scattering angle in the existing light scattering techniques and thus enables the determination of aggregate size with a higher spatial resolution. Coupled with multi-wavelength line-of-sight attenuation measurements, the proposed Horizontal Planar Angular Light Scattering at 532 nm was found able to provide radial profiles of aggregate size, number and diameter of primary spheres, soot volume fraction, and number density in a laminar axisymmetric coflow ethylene/air diffusion flame established over a Gülder burner. The spatial variation of soot optical properties associated with soot maturity was considered in data analysis.

Keywords: Planar angular light scattering, Axisymmetric flames, soot maturity, Line-of-sight attenuation, RDGFA

*Corresponding authors.*E-mail addresses:* yon@coria.fr

1. Introduction

Soot formation and oxidation mechanisms are still not completely understood and very challenging to model. Yet, it is becoming imperative to design energy systems that are cleaner and have less impacts on human health and on the environment. To this end, numerical simulation plays a vital role to speed up the design and optimization processes. To gain improved fundamental understanding of soot formation mechanisms and to validate soot models, it is essential to obtain complete and robust databases of soot properties in well-controlled and highly stable laminar target flames. Such efforts have been continuously made in the last four decades through developing sophisticated *in-situ* optical techniques. Among these techniques, Laser Induced Incandescence (LII) has received widespread attention [1].

LII enables the determination of soot volume fraction in complex, transient environments [2] or in very low sooting flames [3]. The LII signal temporal decay rate can be interpreted in terms of soot primary sphere diameters [4, 5].

By conducting LII measurements using two different laser wavelengths, it is possible to determine the ratio of soot absorption functions at the two laser wavelengths, which in turn can be linked to the soot maturity [6–8]. The line-of-sight attenuation (LOSA) and spectral soot emission (SSE) methods are also often used in laminar axisymmetric flames to determine the soot volume fraction and flame temperature [9]. A recent study has shown that LOSA measurements at different wavelengths in the visible and near infrared can provide instructive information on the soot maturation process with a high spatial resolution [10]. Measurement of the volume fraction of incipient soot is extremely challenging due to the very low volume fraction associated with the very small incipient soot particles and their weak absorption in the visible. Although the soot aggregate size is important to validate the aggregation and oxidation mechanisms modeled by Population Balance Equation [11, 12] or discrete element methods [13, 14], the above optical techniques are not able to provide information of soot aggregate size, morphology, and aggregate number density, which are also important quantities to fully characterize soot. To complement the measurements of LII, LOSA, or SSE, the soot aggregate size information has often been obtained through an *ex-situ* method through soot sampling in the flame [15, 16]. However, sampling of nanoparticles is intrusive in nature and can alter the structure of the flame [17, 18]. Moreover, the particle aggregation process can occur

in the sampling line as well as smaller particles can be lost by deposition [3]. Finally, the aerosol sizing instruments provide the particle size distributions in either mobility or aerodynamic diameter that have to be interpreted to obtain aggregate size, such as gyration radius, since soot particles are not spherical [12]. These considerations suggest that it is necessary to develop *in-situ* techniques to measure soot aggregate size. It has been demonstrated some 40 years ago by Santoro et al. [19] that scattering based techniques are able to provide instructive information on soot size. Köylü and Faeth [20] have shown that the interpretation of scattering measurements of soot particles should be performed by a dedicated theory of light interaction with fractal aggregates called RDGFA [21], but not by Mie theory.

The reader is invited to refer to Sorensen [22] for more details about that the RDGFA theory. This approach has been extensively used to interpret light scattering measurements of sooting flames [23–25]. Wang and Sorensen [26] have shown the reliability of the RDGFA theory for TiO2 and SiO2 aggregates and later Chakrabarty et al. [27] for carbonaceous chain aggregates. It has also been shown in some studies that there is good agreement between the size of both aggregates and primary spheres obtained by light scattering compared to Transmission Electron Microscopy image analysis [28–30]. However, light scattering techniques have been less favored in recent years compared to LII. Indeed, the current angular light scattering method remains challenging in the sense that the change of scattering angle is accompanied by a change in the measurement volume and thus suffers the problem of a significantly reduced spatial resolution for small and large scattering angles, leading to large uncertainties in the inferred soot aggregate sizes in diffusion flames where physical and chemical quantities display high spatial gradients.

Nevertheless, the light scattering techniques are still being improved. An integrated system enabling the measurement of soot size distribution with high temporal resolution has been developed by Oltmann et al. [31]. Bouvier et al. [32] and Zhang et al. [33] have shown the potential of exploiting the spectral dependency of the scattered light. The vertical planar configuration in an ethylene diffusion flame [34, 35] and in premixed 1D flat flame (McKenna-type burner) [36] has been developed in order to provide a planar description of the soot size. Finally, the light scattering based techniques have been applied in more and more challenging configurations [37, 38] and some efforts have been made to improve the light scattering theories [39, 40] and the inversion algorithms to accurately recover aggregate size distribution [27, 41, 42]. These studies illustrate the potential of light scattering tech-

niques and coupled techniques based on light scattering and other optical diagnostics [43, 44].

Up to now, 2D Multi Angle Light Scattering is the technique providing the aggregate size with the finest spatial resolution [36]. However, the data processing is not simple. Indeed, as explained by Ma and Long [34], the observed image of the laser light sheet interaction with the flame "became narrower in shape and the signal on each pixel was increased due to an increased sample volume". In other terms, the image resolution and the volume of measurement change with the scattering angle when rotating the camera around the burner. Then, an intensity calibration and a correction of distortion of the images are required [34, 36]. These corrections may have an impact on the spatial resolution of such planar light scattering technique.

The present work intents to overcome the issue of scattering angle dependent measurement volume and to improve the spatial resolution of laser-based light scattering technique. This is achieved by the use of an unconventional horizontal laser sheet configuration and the application of this technique is demonstrated in a laminar axisymmetric diffusion flame. This technique enables the determination of soot aggregate size distribution with a high spatial resolution along the radial direction. The coupling of this technique with multi-wavelength LOSA enables the determination of additional information, such as volume fraction, number density, and primary particle size. The combined technique also permits to analyze the data by taking into account the maturity dependence of soot optical properties.

2. Experimental setup, theoretical method, and data analysis

2.1. Experimental setup

Figure 1 shows the experimental setup used in this study. The Gülder laminar coflow diffusion flame burner can be accurately moved vertically by means of an Electromechanical cylinder EMC Rexroth. This linear stage facilitates the scanning of scattering measurements at different height above the burner (HAB) with a precision < 10 μm. The laminar coflow diffusion flame is generated by delivering pure ethylene through the central fuel tube of the burner at a flowrate of 0.194 l_n/min. The inner and outer diameters of the central fuel tube are 10.9 mm and 12.7 mm, respectively. The oxidizer is ambient air introduced through the co-annular region of the burner between the central fuel tube and the 90 mm inner diameter of the oxidizer port at

150 l_n/min. These conditions result in a stable laminar diffusion flame with a visible flame height of 75 mm.

Unlike conventional light scattering techniques that utilize a laser beam or a laser sheet orthogonal to the camera axis, the present setup employs a horizontal laser sheet that is wider than the largest flame diameter. This original arrangement can overcome the issue of scattering angle dependent measurement volume at the expense of conducting Abel inversion as shown below. To apply the horizontal planar angular light scattering (HPALS) technique proposed in this study, a Quantel Brillant Easy laser pumped at 1064 nm and frequency-doubled at 532 nm is employed. The laser is set for a maximum energy peak per pulse of 185 mJ at 10 Hz with a pulse duration of 4 ns (FWHM). The laser output energy is modulated by an internal polarized based attenuator. It is first spatially filtered by using a pin-hole (2.44 mm diameter) in order to preserve the uniform region of the laser beam. Two 532 nm dichroic mirrors M1 (CVI Y2-1025-45-A) and M2 (CVI Y2-2037-45) are employed to modify the direction of the laser beam and laser sheet, respectively. A variable dielectric attenuator VA1 (Laseroptik L-01543) is used to redirect a part of the laser beam toward a power meter (Coherent PowerMax Model PM10) in order to measure the energy of laser beam during each measurement.

The horizontal laser sheet is formed by the combination of three cylindrical lenses, a plano-concave L1 (f=−40 mm, CVI SCC-20.0-20.3-C), a plano-convex L2 (f=300 mm, Thorlabs LJ1996L1), and a second plano-convex L3 (f=500 mm, Thorlabs LJ1144L2). This horizontal laser sheet is then projected across the flame with a width of 15 mm (larger than the maximum flame diameter ∼10 mm). A reasonably uniform thickness is obtained with 141 μm (corresponding to 2σ) measured with a Precision Beam Profiler (Photon Inc. Model 2323 USB 2.0 Camera). Note that the polarization state is orthogonal to the laser sheet, i.e., in the vertical direction in Fig.1.

The detection system is mounted on a motorized rotating arm (Danaher motion N33HRLG-LEK-M2-00) to enable the signal collection at different scattering angles designated by θ (see Fig. 1). The optical collection is composed of a vertical polarizer P1 (Linear Pola 49 mm, second white arrow in Fig.1) and a long distance microscope system (Infinity CF2+basic unit) mounted with an 1.5 cm extension ring on an ICCD camera (PI-MAX-4, model PM4). The internal laser PTU is employed to trigger the camera to capture the scattering signal for each laser pulse. In order to limit the collection of the flame natural emission, the ICCD exposure time is reduced to

14.88 ns.

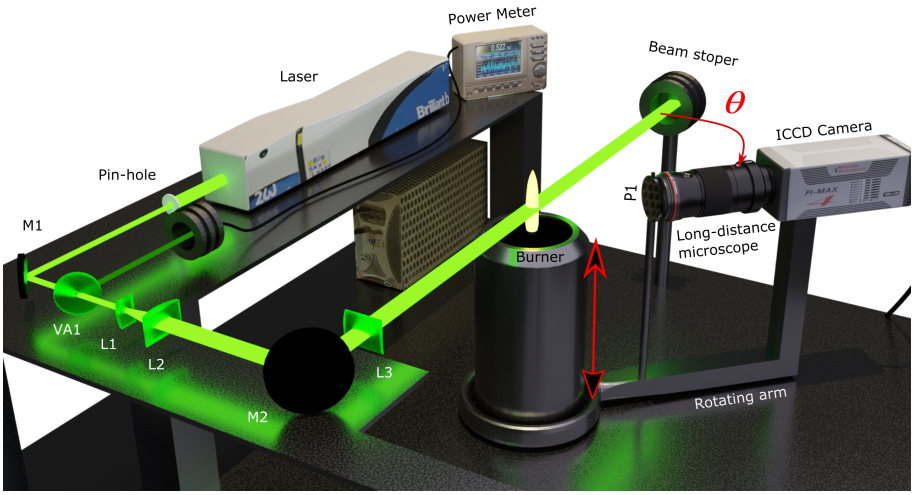

Figure 1: Experimental setup: The horizontal laser sheet is arranged to cross the flame. The Height Above the Burner can be modified (red arrow) as well as the scattering angle (θ) by rotating the camera around the flame axis. M1 and M2 are two dichroic mirrors, L1, L2 and L3 are respectively a cylindrical, plano-concace, and plano convex lenses. VA1 is a variable dielectric attenuator and P1 is a polarizer.

2.2. Raw data treatment

Up to 2000 images of 1024×1024 pix^2 are accumulated or averaged per condition depending on the signal intensity. The image resolution is ~ 51 pix/mm, and the field of an image can cover the width of the flame as depicted in Fig. 2-A. Also, in this figure the region of interest (ROI) is highlighted by the white rectangle of dashed-line. This ROI corresponds to the image of scattering signal of the horizontal laser sheet captured by the ICCD at HAB = 30 mm and a scattering angle of 14.9°. The same ROI is also employed with the laser off in order to obtain the background. The profiles after subtracting the aforementioned background are divided by the corresponding laser energy, the number of accumulations, and the camera gain. The laser sheet uniformity was checked and it was found quite good. The lateral bumps observed in Fig. 2-A are likely caused by multiple scattering in the dense regions (high soot concentration) of the flame. This phenomenon, which is not considered in the present analysis, will be investigated in our future research. Nevertheless, its contribution is considered very small (please

note that the scattering intensity is displayed in log scale). Fig. 2-B presents two normalized profiles of two different scattering angles at a given HAB. To avoid a noisy deconvolution, the Python "Savgov filter" (polynomial of order 2 and 31 elements in the averaging window and mirror boundary) is used. The PyAbel's "Hansenlaw" method [45] is used to deconvolute the experimental profiles (Abel inversion, see the dash curves in Fig. 2-B). The obtained radial profile is re-convoluted and compared to the acquired signal to check the validity of the deconvolution process (the continuous curves in Fig. 2-B). The re-convoluted scattering signal profiles are in very good agreement with the measurements.

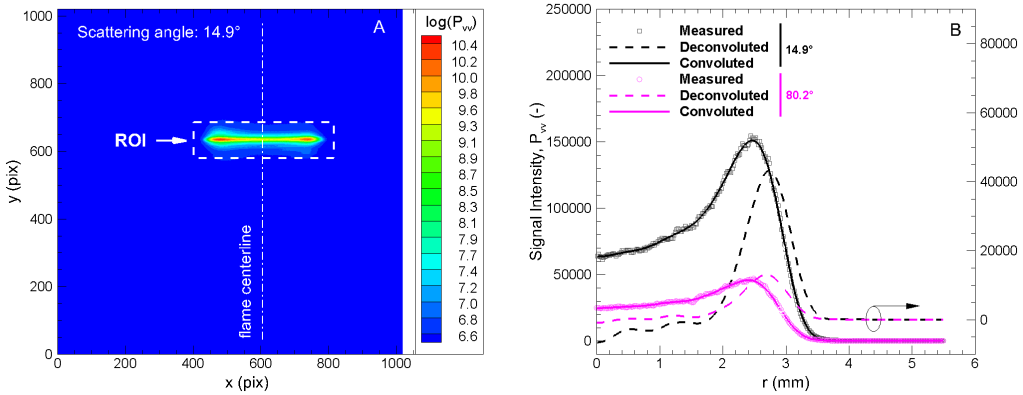

Figure 2: A typical light scattering image (left plot) and profiles captured at HAB = 30 mm and at two angles, 14.9° (or $q = 0.0030$ nm^{-1}) and 80.2° (or $q = 0.0152$ nm^{-1}) (right plot): (A) Raw scattering signal field and ROI employed (at a scattering angle of 14.9°) and (B) Measured scattering signal profile (symbols), deconvoluted profile (Abel inversion in dash curves), and re-convoluted profiles using the deconvoluted signal (continuous).

3. Light scattering theoretical background

3.1. Determination of the absolute scattering coefficient

As illustrated in Fig. 3, the radiative power of scattered light reaching the detector by molecules or particles from an elementary volume dV located at position M and exposed to a planar incident light source with power density I_0 (in W/m^2) can be expressed as,

$$dP_{vv} = I_0 \overline{\frac{dK_{vv}}{d\Omega}} \Omega dV, \tag{1}$$

where $\overline{\frac{dK_{vv}}{d\Omega}}$ is the population averaged differential scattering coefficient for vertical-vertical polarization and Ω the solid angle related to the detection aperture. The elementary volume can be expressed as $dV = dxdydz$, where x and y are respectively the positions along the detector and orthogonal to the detector (see Fig. 3) and z is the position along the flame height. The term $dS = dxdz$ corresponds to the elementary surface of the pixel of the ICCD camera which collects the scattered light originated from dV at the scattering angle θ. This elementary volume can also be expressed as $dV = \frac{rdrdS}{\sqrt{r^2-x^2}}$ with r being the distance of M from the flame center line.

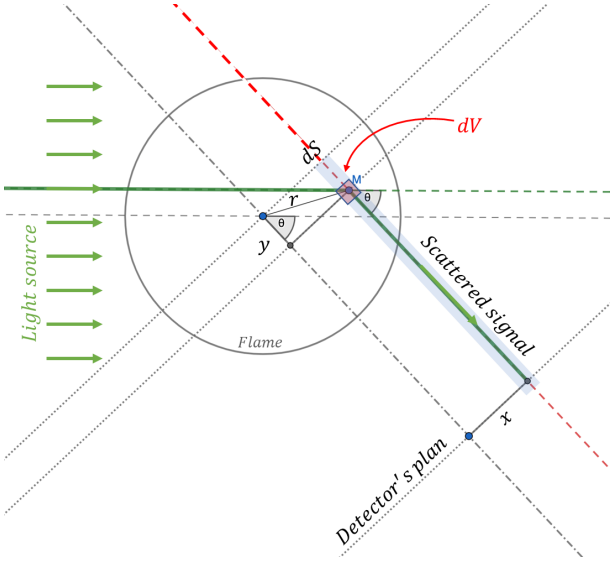

Figure 3: Schematic of the HPALS principle (top view).

By assuming negligible laser energy attenuation and self absorption of the scattered signal, the collected signal at position x on the detector can be expressed as an Abel transform of the averaged scattering coefficient, namely the integrated scattering signal along the cord corresponding to position x:

$$P_{vv} = I_0 \Omega dS \times \underbrace{2\int_x^{\infty} \overline{\frac{dK_{vv}}{d\Omega}} \frac{r}{\sqrt{r^2-x^2}} dr.}_{Abel\ transform\ of\ \overline{\frac{dK_{vv}}{d\Omega}}} \tag{2}$$

It should be pointed out that laser energy attenuation and signal trapping at 532 nm in the ethylene flame studied in this work may not be negligible at

flame heights where soot volume fractions are fairly high. Nevertheless, such effects are neglected in the first attempt to demonstrate the capabilities of the HPALS technique and will be evaluated and taken into account in future studies.

Thus, for each scattering angle imposed by the angular position of the camera, the radially-resolved scattering coefficient can be retrieved by a simple inverse Abel transform (Ab^{-1}) of the convoluted scattering signal profile acquired over the entire range of x,

$$\overline{\frac{dK_{vv}}{d\Omega}} = Ab^{-1}\left(\frac{P_{vv}}{I_0 \Omega dS}\right). \tag{3}$$

In order to determine the absolute value of the averaged scattering coefficient, a calibration of the detection system is necessary. In this study the calibration is performed by measuring the scattered signal produced by a free jet of ethylene P_{vv,C_2H_4}. At ambient conditions, the molecule density and the corresponding scattering cross section [22] are known. The resultant scattering coefficient is found to be $K_{vv,C_2H_4} = 8.92 \times 10^{-6}\ m^{-1}$.

It is noticed that the collected scattering signals from the flame soot as well as from the ethylene jet are systematically normalized by the corresponding laser intensity, number of accumulated images and camera gain, the absolute scattering coefficient of soot is then given by:

$$\overline{\frac{dK_{vv,soot}}{d\Omega}} = K_{vv,C_2H_4} \times \frac{Ab^{-1}\left(P_{vv,soot}\right)}{Ab^{-1}\left(P_{vv,C_2H_4}\right)}. \tag{4}$$

The measured profile (P_{vv,C_2H_4}) and its deconvolution $Ab^{-1}\left(P_{vv,C_2H_4}\right)$ are given in Appendix A.

3.2. Interpretation of scattering coefficient based on the RDGFA theory

For an ensemble of monodisperse aggregates and under conditions where the RDGFA theory is considered valid [22], the aggregate differential scattering coefficient can be expressed as,

$$\frac{dK_{vv,soot}}{d\Omega} = N_{agg}\frac{9\pi^2}{\lambda^4}F(m)V_{agg}^2 f(qR_g, D_f). \tag{5}$$

where N_{agg} and V_{agg} are respectively the aggregate number density and the individual aggregate volume, m is the soot complex refractive index, $F(m) =$

$|\frac{m^2-1}{m^2+2}|$ is the scattering function of m, λ is the incident laser wavelength, f is the structure factor, R_g is the gyration radius (the radius of an equivalent sphere having the same inertia moment), and $q = \frac{4\pi}{\lambda} sin\left(\frac{\theta}{2}\right)$ is the magnitude of scattering wave vector. Symbol D_f is the aggregate fractal dimension. The scaling law correlating the aggregate volume to its gyration radius is expressed as

$$N_p = \frac{V_{agg}}{V_p} = k_f \left(\frac{D_g}{D_p}\right)^{D_f}, \tag{6}$$

where N_p is the number of primary spheres, V_p is the volume of primary sphere, $D_g = 2R_g$ is the aggregate gyration diameter, D_p is the diameter of the primary spheres, k_f is the fractal prefactor (assumed equal to 2.2 in the present study, consistent with TEM measurements, e.g. [46]). We will also assume a typical value of $D_f = 1.77$ for flame-generated soot, which is also the value of aggregates generated by diffusion-limited cluster aggregation (DLCA).

The structure factor formulated by Dobbins and Megaridis [47] is used in the present study because it has been shown to be accurate for the determination of the aggregate gyration radius based on light scattering at 532 nm even when considering the aggregate internal multiple scattering [40].

For polydisperse aggregates, by introducing the soot volume fraction as $f_v = N_{agg} \times \overline{V_{agg}}$ and by using the factal scaling law (Eq. 6), the population averaged scattering coefficient can be expressed as,

$$\overline{\frac{dK_{vv,soot}}{d\Omega}} = \underbrace{\frac{9\pi^2}{\lambda^4} F(m) f_v \frac{\overline{V_{agg}^2}}{\overline{V_{agg}}}}_{Amplitude} \underbrace{\frac{\overline{R_g^{2D_f} f(qR_g, D_f)}}{\overline{R_g^{2D_f}}}}_{Size\ dependent}. \tag{7}$$

In this expression, we can distinguish the amplitude of the signal, which corresponds to the magnitude of the forward scattering signal ($\theta = 0$), and the ratio $\frac{\overline{R_g^{2D_f} f(qR_g, D_f)}}{\overline{R_g^{2D_f}}}$ that contains the angular dependence through the q parameter. In this study, the angular dependence term is interpreted in terms of aggregates size distribution. Moreover, the scattering amplitude is coupled with LOSA measurements (see [10]) and interpreted in order to determine the aggregates volume, density and primary sphere diameter.

3.3. Soot aggregate size distributions

Interpretation of Eq. 7 requires some *a prior* knowledge of the size distribution density probability function. In the present study, three assumed distributions are considered, namely Monodisperse, Lognormal and Self-Preserving.

Due to the large particle number density and fairly high temperatures in flames, it is highly unlikely that the aggregate sizes are monodisperse. Nevertheless, this case is considered in order to test the sensitivity of the methodology proposed to the assumed shape of aggregate size distribution and to the magnitude of polydispersity. The Lognormal size distribution of soot aggregates is considered because it is usually observed when expressed in mobility diameter. Nevertheless, there is no theoretical basis to this empirical observation in particular when the aggregate size is expressed by gyration diameter. On the contrary, aggregation mechanisms for fractal aggregates suggest a self-preserving size distribution [48]. Sorensen [22] pointed out that this distribution can shorter the tail of the distribution for larger aggregates compared to the Lognormal distribution, which is suspected to overestimate the moments used for the evaluation of $\overline{V_{agg}}$, $\overline{V_{agg}^2}$, $\overline{R_g^{2D_f} f}$ and $\overline{R_g^{2D_f}}$ in Eq. 7.

The lognormal distribution is governed by the geometric diameter D_{geo} and the geometric standard deviation σ_{geo}. The former is not so different from the modal diameter of the distribution (most probable size). Caumont-Prim et al. [30] reported $\sigma_{geo} = 1.7$ based on angular light scattering measurement in an ethylene flame for mature soot. The same author found 1.6 when applying the technique on soot at the exhaust of a miniCAST generator. The latter value (1.6) will be considered here since the exhaust of miniCAST provides a uniform soot source avoiding issues related to the spatial resolution of the conventional light scattering technique. This is also in agreement with the values reported by Bouvier et al. [32]. However, it is noticed that some authors considered larger values of the geometric standard deviation [29, 48].

The self-preserving distribution is governed by a $\widetilde{D_g}$ and by the self-preserving homogeneity coefficient λ_{SP}. The latter parameter controls the shape of the distribution. It has been reported to vary over a range of physical values between -0.5 and 0.5 depending on the aggregation mechanisms, which are principally driven by the primary sphere diameter (positive when ballistic and negative when diffusive). In the present study, we hypothesize that this parameter takes the value of null ($\lambda_{SP} = 0$) as a result of aggregation occurring in the transition regime with a typical primary particle diameter

about 20 nm (see [48]). The size driving parameter $\widetilde{D_g}$ is related to a moment of the size distribution at power D_f, indeed $\widetilde{D_g} = \left(\overline{D_g^{D_f}}\right)^{1/D_f}$ [48]. In consequence, this parameter becomes larger as the aggregates are increasingly more polydisperse.

A theoretical analysis of the self-preserving distribution, which has been shown to be a generalized gamma function [48], has shown that $D_{g,modal} = \widetilde{D_g}\left(1 - \frac{1}{D_f(1-\lambda_{SP})}\right)^{1/D_f}$ with $D_{g,modal}$ being the mode of the distribution. In the present case where D_f and λ_{SP} are fixed respectively at 1.77 and 0, one can find $\widetilde{D_g} = 1.57 \times D_{g,modal}$. Thus, it is important to keep in mind that $\widetilde{D_g}$ is consistently larger than the most probable gyration diameter (mode of the distribution).

The analytical expressions for $\overline{R_g^{2D_f} f}$ and $\overline{R_g^{2D_f}}$ under the hypothesis of Monodisperse, Lognormal and Self-Preserving distributions are presented in Appendix B.

4. Results and Discussion

4.1. Results at HAB = 30 mm

Figure 4 presents in black dots the radially-resolved scattering signals expressed in K_{vv} measured at 22.4°, 33.9°, 51.1°, 80.2°, 90°, 119.8° and 148.1°, for HAB = 30 mm through Abel inversion. The scattering wave vector q is preferred over the direct use of scattering angle for the representation of angular dependence of scattering because this parameter is used in the RDGFA theory. The scattered intensity decreases with increasing q, in particular for large aggregates. Thus, at a given radial position r, the aggregate size distribution can be obtained by fitting the curve in the q direction (e.g. the red arrow in the graph). It should be pointed out that the aggregate size distribution determined does not depend on the amplitude of K_{vv} (green arrow in graph). This point will be explained after.

The results of the aggregate size distribution parameters are reported in Fig. 5. In this figure, the points of red-circle are the gyration diameters of Monodisperse size distribution (D_g), while the points of green-star and blue-square are respectively the $\widetilde{D_g}$ and D_{geo} for the self-preserving and lognormal distributions.

It is interesting to see that $\widetilde{D_g}$ at power D_f corresponds to the population average gyration diameter at power D_f ($\widetilde{D_g}^{D_f} = \overline{D_g^{D_f}}$). Due to the

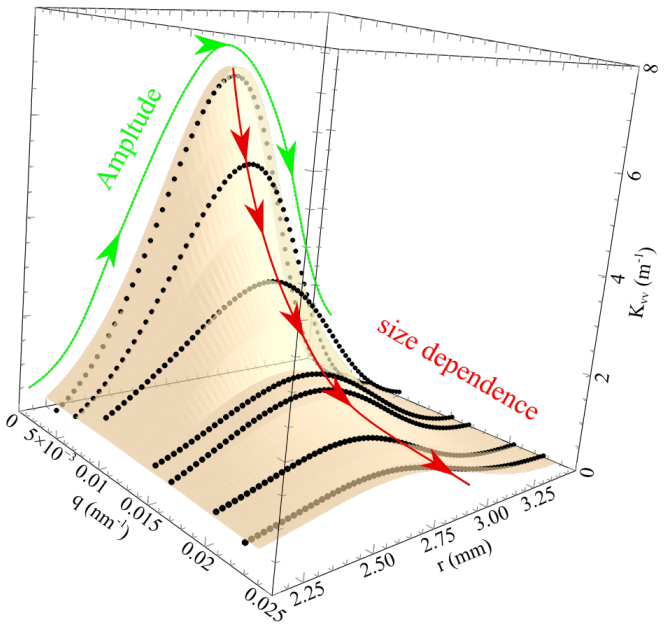

Figure 4: Radial and angular distribution of the scattered signal at HAB = 30 mm after Abel inversion and expressed in terms of K_{vv}. The angular dependence of scattering is expressed through $q = \frac{4\pi}{\lambda} sin\left(\frac{\theta}{2}\right)$, which is the magnitude of the scattering wave vector. The measured scattering signal is presented in black dots after the fitting process generating a continuous surface.

polydispersity, those parameters are lower than the equivalent gyration diameter under the assumption of monodisperse aggregates. Nevertheless, the assumption of monodisperse soot aggregates is clearly unrealistic in flames.

Therefore, we consider the lognormal or self-preserving hypothesis more representative of soot aggregates. $\widetilde{D_g}$ is found to be somewhat larger than D_{geo} even though the self-preserving size distribution is lower than the lognormal one for small aggregates (see the inset of Fig. 5). This behavior is attributed to the definition of $\widetilde{D_g}$ which represents a moment of power D_f, whereas D_{geo} is the median diameter.

It is interesting to notice that larger aggregates are found at a radial position between $r = 2.9$ and 3.0 mm whereas the signal amplitude starts to decrease at this radial distance at HAB = 30 mm (see Fig. 4).

The band that bounds each curve by dotted lines in Fig. 5 indicates the fitting quality. The band height is evaluated by considering the variance of

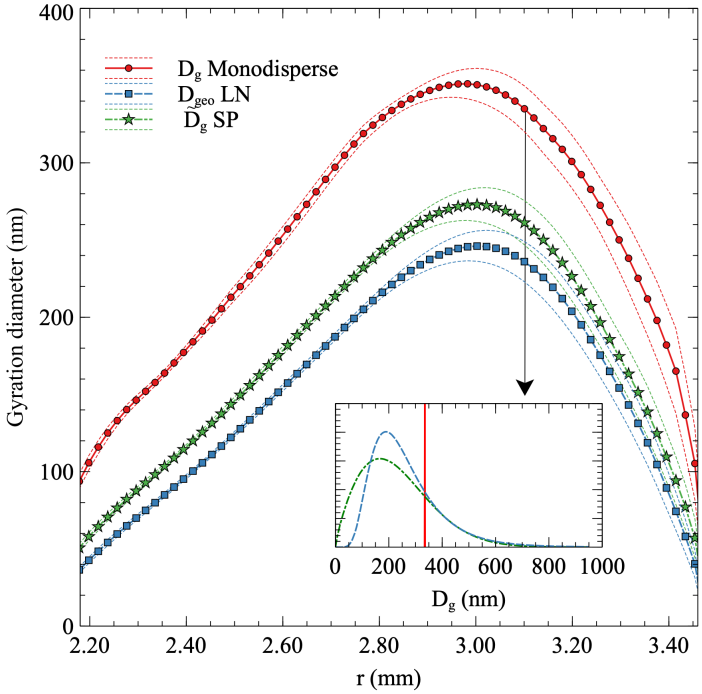

Figure 5: Radial profiles of soot gyration diameter distribution parameters at HAB=30 mm. The three profiles correspond to monodisperse, logNormal ($\sigma_{geo} = 1.6$), and self-preserving ($\lambda_{SP} = 0$) density probability functions. The bands between the dotted lines around each curve are an indication of the reliability level of the results. The inset illustrates the three aggregate size distributions at $r = 3.1$ mm.

experimental measurements around the fitted model. It should be noticed, however, that the band height is not the measurement uncertainty since it is very difficult to evaluate the latter. Nevertheless, we can consider the band height as a proxy to the measurement uncertainty. In consequence, we can see the uncertainty relative to the soot aggregate size is larger on the outer edge of the flame wing. This is in part caused by the lower signal intensity in this region. For $r \leq 2.8$ mm, the fitting quality is slightly better for the Lognormal and the Self-Preserving distributions than the Monodisperse one. For the two polydisperse distributions (LN and SP) the fitting quality is essentially the same over the entire radial range at HAB = 30 mm, suggesting that it is impossible to say which distribution is a better representation of soot aggregate size based on the fitting quality alone.

In addition to the determination of aggregate size distribution parameter, the fitting process of the recorded signals (Fig. 4) also enables an extrapolation of the forward scattering intensity ($K_{vv}(0^o)$) corresponding to the amplitude term in Eq. 7. The results are reported in Fig. 6-A for the three assumed aggregate size distributions. $K_{vv}(0^o)$ is clearly affected by the hypothesis of the aggregate size distribution primarily in the amplitude but also slightly in the radial position of the peak.

The forward scattering intensity is determined by the soot volume fraction f_v, scattering function of the refractive index $F(m)$, and ratio of aggregate volume moments $\overline{V_{agg}^2}/\overline{V_{agg}}$. In order to extract the moment ratio, we divide the amplitude term by f_v and $F(m)$, which are reported in Fig. 6-B at HAB = 30 mm. The volume fraction f_v has been determined by LOSA measurements at multiple wavelengths (500, 532, 660 and 810 nm) in order to take into account the influence of maturity dependence of soot optical properties [10]. The value of $F(m)$ is derived from the spectral dependence of absorption function $E(m)$, which in turn provides the soot maturity index and finally the absolute absorption function $E(m)$ (see [10]).The same methodology can be used to infer the scattering function $F(m)$ in the present study (see Appendix C by utilizing the relationship between maturity index and $F(m)$). Nevertheless, it should be pointed out that according to the model used the change of scattering function at 532 nm is fairly weak compared to the change of absorption function (see [10]). Thus, the impact of soot maturity on the scattering function is less pronounced.

Figs. 6-B and 6-A clearly show a shift among the maximum volume fraction (at $r \approx 2.6$ mm), scattered intensity ($r \approx 2.8$ mm) and sharp increase of maturity ($r \approx 2.95$ mm). The corresponding ratio $\overline{V_{agg}^2}/\overline{V_{agg}}$ for the three assumed distributions is reported in Fig. 6-C. This ratio remains almost the same as the average aggregate volume for $r \leq 2.3\ mm$; however, it shifts slightly towards larger values at larger radial positions for polydisperse aggregate distributions. In addition, the ratios for the lognormal distribution are seen to be slightly larger than those of the self-preserving distribution.

The increase in $\overline{V_{agg}^2}/\overline{V_{agg}}$ with increasing r suggests an increase in the average aggregate volume and in the aggregate polydispersity up to the outer edge of the flame. The even higher values of this ratio beyond $r = 3.25\ mm$, where soot volume fraction drops to zero, are unphysical and can be considered a result of noise.

On the other hand, it can be seen from Fig. 6-C that the uncertainty in $\overline{V_{agg}^2}/\overline{V_{agg}}$, which is based on the propagation of error of the amplitude and

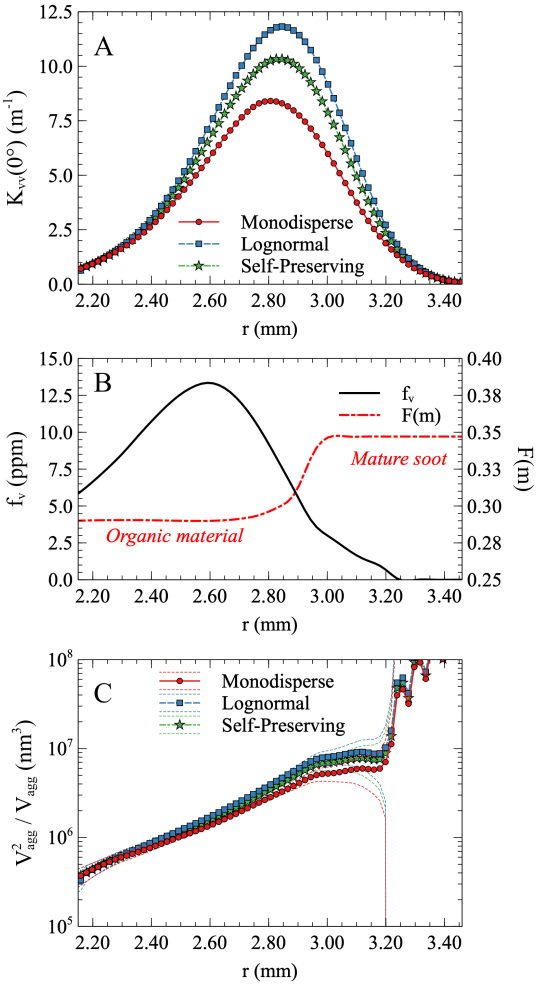

Figure 6: Radial profiles of selected properties of soot particles at HAB = 30 mm. A) Amplitude of the signal extrapolated at forward scattering $K_{vv}(0)$. B) Radial distribution of soot volume fraction f_v and scattering function $F(m)$ according to [10]. C) Ratio of aggregates volumes momentum's $\overline{V_{agg}^2}/\overline{V_{agg}}$. The three profiles in the top and bottom plots correspond to data interpretation for the assumed three aggregate gyration diameter distributions: monodisperse, lognormal ($\sigma_{geo} = 1.6$), and self-preserving ($\lambda_{SP} = 0$).

volume fraction terms, also increases with increasing r due to the decrease of f_v. Up to $r \approx 2.9$ mm, it is not surprising to observe an increase of the aggregate volume since the aggregate size increases (see Fig. 5). However, it is less obvious for the increase in the ratio at larger r where the aggregate size decreases, Fig. 5. This may be interpreted by an increase of the primary sphere radius. Indeed, as shown in Table 1, the representative aggregate volume term (the ratio of aggregate volume moments) depends on not only the aggregate gyration diameter but also the primary sphere diameter D_p. At this point, the aggregate size distribution is already determined thus the radial behaviour of the primary sphere diameter can be established (see Fig 7-A). Because this quantity depends not only on the amplitude and angular variation of the scattered signal but also on the soot volume fraction and the morphological parameters (D_f and k_f), its uncertainty is relatively large. For example, a lower fractal prefactor will cause an increase in the determined primary sphere diameter. Again, the band bounded by two dotted lines around each curve indicates the uncertainty based on error analysis. These curves clearly show large uncertainties in the inner and outer regions of the flame along the radial direction.

It is noticed that the obtained primary sphere diameters are in reasonably good agreement with results reported in the literature. At the same HAB, Botero et al. [49] found by TEM image analysis in a laminar coflow diffusion flame over the Yale burner and fueled with nitrogen diluted ethylene that the primary soot particles have a modal diameter of 21 nm with a high polydispersity. Slightly larger values have been reported by Kempema and Long [35]. In the same burner as in the present study and also for pure ethylene, Cortés et al. [46] also performed TEM image analysis and found at a similar location (HAB = 27 mm) and oxygen index (21%) that the primary soot particles have a geometric mean diameter of 16 nm and a geometric standard deviation of 1.6. Considering that Rayleigh scattering is a process proportional to D_p^6, the results of Cortés et al. [46] can be reanalysed in terms of the optical equivalent primary sphere diameter by using the Hatch-Choate equation (average primary diameter at power 6) to yield 31 nm, in very close agreement with the present results. Indeed, we observe $D_p \approx 32$ nm in the region where the uncertainties are low (see Fig 7-A)).

The region of low uncertainties ($2.6 \leq r \leq 2.85$) displays a locally increasing trend of the primary sphere diameter with increasing r that can be related to the surface growth process. This region also corresponds to the rapid increase in soot maturity as shown by the red dashed curve in Fig 6-B.

Table 1: Analytical expressions for the ratio of aggregate volume moments for monodipserse, lognormal, and self-preserving size distributions.

Distribution	$\frac{\overline{V_{agg}^2}}{\overline{V_{agg}}}$
Mono	$\frac{\pi}{6} D_p^{3-D_f} k_f D_g^{D_f}$
Lognormal	$\frac{\pi}{6} D_p^{3-D_f} k_f D_{geo}^{D_f} e^{(2-\frac{1}{2})D_f^2 ln^2(\sigma_{geo})}$
Self-Preserving	$\frac{\pi}{6} D_p^{3-D_f} k_f \widetilde{D_g}^{D_f} \frac{2-\lambda_{SP}}{1-\lambda_{SP}}$

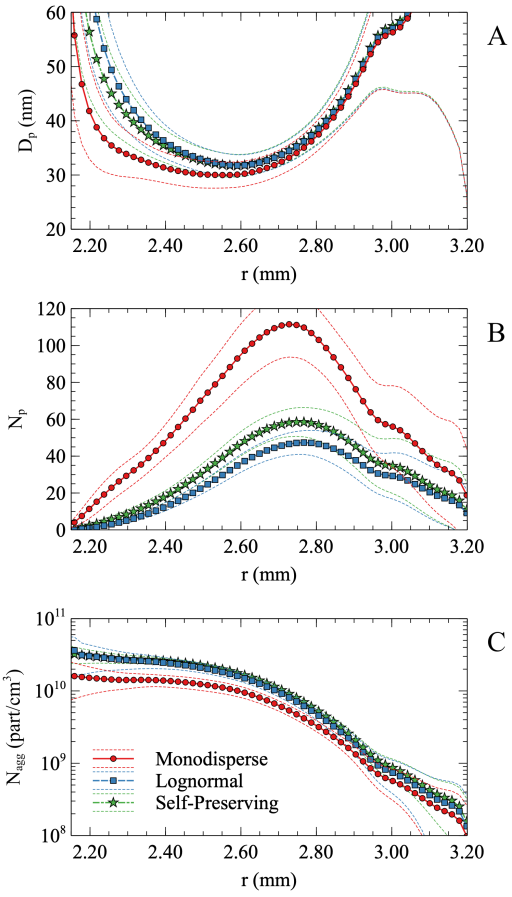

Figure 7: Radial profiles of some soot properties inferred from light scattering measurements at HAB = 30 mm. A) Primary sphere diameters D_p, B) Number of primary spheres per aggregate N_p related to the representative diameter and C) Aggregates number density N_{agg}. The three curves correspond to results for Monodisperse, Lognormal ($\sigma_{geo} = 1.6$) and Self-Preserving ($\lambda_{SP} = 0$) density probability function hypotheses.

In addition, since gyration diameter and primary sphere diameter are determined, we can evaluate the corresponding representative number of primary spheres (N_p) per aggregate employing the fractal law (Eq. 6). The result is reported in Fig 7-B. As already discussed for the gyration diameter, N_p is found to be larger if the aggregates are assume to be monodisperse.

The maximum average number of primary spheres per aggregate (at about $r = 2.74\ mm$) is found slightly shifted toward the flame centerline compared to the maximum representative gyration diameter (at about $r = 3.0\ mm$, Fig 5). This is explained by the increase of the primary sphere diameter due to the surface growth. Assuming lognormal and self-preserving aggregate gyration diameter distributions, the determined maximum average number of primary spheres per aggregate is found to be 46 and 58 at HAB = 30 mm, respectively.

Finally, the aggregate number density can be determined. Indeed, it is evaluated as $N_{agg} = f_v/\overline{V_{agg}}$, with $\overline{V_{agg}} = \pi D_p^{3-D_f} k_f \overline{D_g^{D_f}}/6$ and $\overline{D_g^{D_f}}$ is given in Appendix B according to the type of assumed aggregate size distribution. The results are reported in Fig 7-C. The aggregate number density decreases with increasing r due to aggregation. At radial positions larger than about r = 2.75 mm, we observe a decreasing aggregate number density (Fig 7-C) of smaller aggregates (Fig 7-B), which seems composed of large primary spheres (Fig 7-A).

4.2. Results at different HAB

The methodology described above has also been applied to different heights above the burner. To highlight the capability of the proposed light scattering technique and focus on the measured soot properties in the laminar diffusion flame, we only report below the results based on the hypothesis of self-preserving aggregate size distribution, which is supported by theoretical considerations as mentioned in Section 3.3. It is also useful to recall that the corresponding governing parameter $\widetilde{D_g}$ is larger than the modal diameter of the distribution by a factor 1.57, which results from its moment at a power D_f (see discussion in Section 3.3). Therefore, the corresponding average number of primary spheres per aggregate will be also slightly larger as seen in Fig 7-B.

Figures 8 and 9 report respectively the radial profiles of the self-preserving governing parameter $\widetilde{D_g}$ and the corresponding average number of primary spheres per aggregate N_p at different HAB. The corresponding uncertainties

are represented by the error bars. Clearly, an intense particle aggregation takes place along the flame wing region up to about HAB = 45 mm, followed by a significant decrease of aggregate size at higher HAB. Indeed, simulations performed with the CoFlame code [50] (reported in Appendix D) indicate that particle nucleation, coagulation, and surface growth via surface reactions (HACA) and PAH adsorption processes govern soot production at the lower part of the flame, leading to increased number and diameter of primary particles. These particles are convected downstream where the oxidation processes by OH radicals and O_2 molecules are dominant, causing a decrease in their size and eventually complete oxidation.

To our knowledge, there have been no studies of *in situ* determination of the aggregates size in the flame wing region of a pure ethylene diffusion flame established over the Gülder burner. Therefore, it is challenging to directly compare our present results with those of previous studies. Kempema and Long [35] applied 2D-MALS (multi-angle light scattering) in a nitrogen diluted ethylene flame (20%C_2H_4 and 80%N_2) over the Yale coflow burner and found similar profiles. The monodisperse equivalent gyration diameters they reported was about 440 nm, which is much smaller that the maximum values reported in the present work. However, it should be noted that for larger aggregates ($\widetilde{D_g} \geq 200\ nm$), the fractal dimension can affect the size measurement since part of the collected signal emanates from the power-law regime. Thus, the uncertainty associated with the largest diameters, and thus in particular for HAB = 45 mm, can become significant. Moreover, the different fuels and burners between our work and previous studies may largely explain the difference. Finally, we believe that the present technique offers a greater spatial resolution, enabling to properly resolve the aggregate sizes in the flame region of high gradients. Indeed, we show in Appendix E that the classical 2D-MALS can underestimate the peak gyration diameter detected at HAB = 40 mm by about 100 nm due to the change of measurement volume with the scattering angle. Nevertheless, this strong effect seems to appear only in the presence of large spatial gradients of aggregate size distribution parameter.

The largest aggregates in terms of $\widetilde{D_g}$ are found at HAB = 40 mm, whereas larger values of N_p seem to be at HAB = 55 mm. This difference may be explained by the smaller primary spheres at HAB = 55 mm (see Figure 10). Kempema and Long [35] reported median numbers of monomers per aggregate between 47 and 71 along the centerline, and between 14 to 16 along the wing of a flame established over the Yale coflow burner. Although

the presently reported values are larger than those of Kempema and Long [35], it should be noticed that in addition to the different flame conditions the present results correspond to the number of primary sphere of the representative size parameter $\widetilde{D_g}$, which is not the median parameter reported by Kempema and Long [35].

Due to the large uncertainties related to the primary sphere diameter determination, we only report in Figure 10 the representative values along HAB. These values are the primary sphere diameter whose uncertainty is the lowest in the radial profile at the given HAB. The overall decreasing trend in the representative primary sphere diameter above HAB = 50 mm shown in this figure confirms the strong oxidation process in the upper part of the flame, which is also qualitatively observed from the predictions of the simulated flame (see Appendix D). The results are also in reasonably good agreement with the TEM image analysis reported in [35].

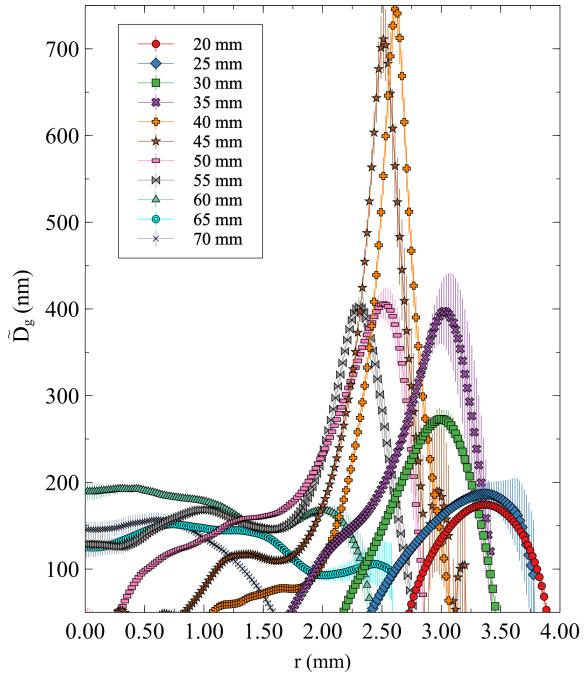

Figure 8: Radial profiles of the aggregate size distribution parameter in the self-preserving distribution assuming ($\lambda_{SP} = 0$) at different HAB.

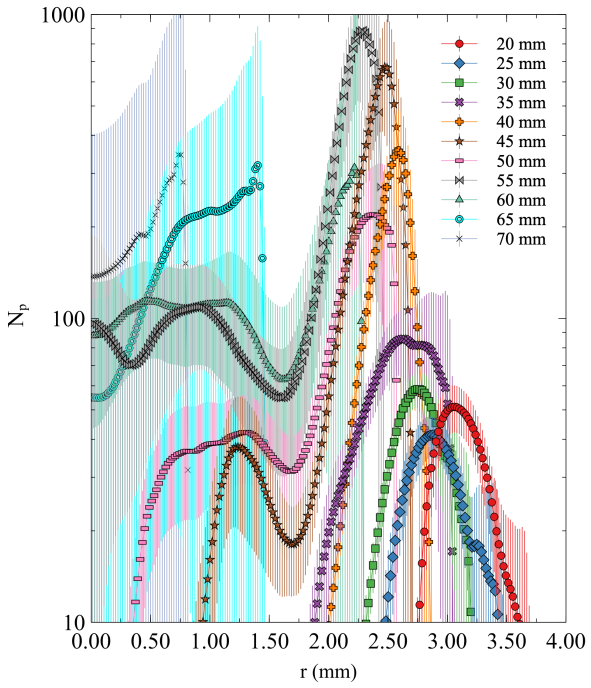

Figure 9: Radial profiles of the average number of primary spheres per aggregate at different HAB.

At low HAB, soot is present only in the flame wing region. With increasing HAB, soot starts to appear in the flame centreline region. At upper part of the flame ($55 \leq HAB \leq 70$ mm), the aggregate size seems relatively uniform in the centerline region within about $r \leq 1.5$ mm. Aggregation seems less intense in this region compared to the outer flame edge. Nevertheless, at the flame centerline large aggregates can be found at HAB = 60 mm (up to about 200 nm) but then decrease to about 150 nm at HAB = 70 mm. This decrease is mainly caused by the decrease of primary sphere diameters while the number of primary spheres still increases. Because this region is marked by a strong reduction of soot material (decrease of volume fraction shown in Appendix C), we can speculate that the soot oxidation in this region of the flame is likely a surface process which mainly reduces the diameter of the primary spheres. Moreover, the aggregation process seems to compensate the possible fragmentation process to some extent.

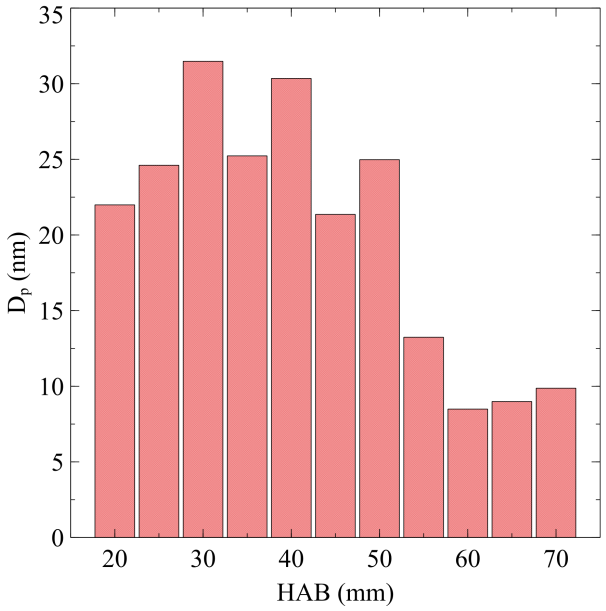

Figure 10: Variation of the representative primary sphere diameter along HAB. The representative primary sphere diameter at each HAB is the value whose uncertainty is the lowest.

Figure 11 presents the radial profiles of aggregate number density at different HAB. The vertical bars represent the uncertainty for each value of N_{agg}. The gradient of this parameter remains very large on the flame wings

up to about HAB = 50 mm, above which soot particles in the centerline region can be detected.

Although some soot particles in the centerline region may be convected from the outer region, soot particles in this region are believed to be mainly composed of nucleation soot with smaller aggregates and immature (lower $E(m)$ and $F(m)$). In this region, the number density is seen to be between 3×10^{10} and 8×10^{10} particles/cm^3, in good agreement with [23, 51] which reported $N_{agg} \sim 10^{10}$ cm^{-3} in similar ethylene diffusion flames.

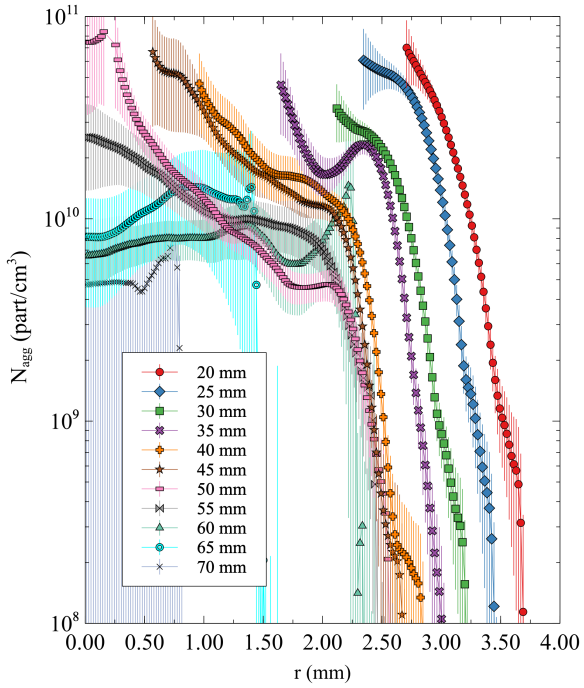

Figure 11: Radial profiles of the aggregates number density at different HAB.

5. Conclusion and perspectives

The present experimental investigation complements our recent study using a multiple-wavelength LOSA analysis for the determination of soot volume fraction and maturity in a laminar coflow ethylene/air diffusion flame produced using a Gülder burner. In the present work, the spatial distribution of aggregate size is determined by elastic angular light scattering.

The originality of the proposed technique lies in optical setup using a laser sheet arranged horizontally through the flame and we named this method the Horizontal Planar Angular Light Scattering (HPALS). This setup avoids the issues related to a significant change of the measurement volume with the scattering angle making the conventional light scattering techniques challenging to apply to flames where soot properties display strong gradients.

The Horizontal Planar Angular Light Scattering technique introduced in this work enables a description of soot characteristics with an extremely high spatial resolution, though it is necessary to conduct Abel inversion.

The coupling of HPALS with LOSA enables a comprehensive description of soot volume fraction, size (aggregate and primary sphere), and number density. The limitation of this technique is that it can only be applied to axisymmetric laminar flames. The coupling of HPALS and multi-wavelength LOSA paves the way to provide a more complete description of soot properties and hence helps improve our understanding of soot formation and oxidation mechanisms. The present work also enables a complete database of soot properties that is useful for validation of soot models able to consider the aggregation mechanisms. Additionally, the high spatial resolution of HPALS allows to improve and validate the coagulation models in regions of steep gradients where the conventional light scattering techniques cannot properly resolve soot properties, such as N_{agg} and N_p. In summary, the combination of HPALS and multi-wavelength LOSA offers a powerful diagnostic tool to provide improved description of soot properties related to aggregate size.

Acknowledgments

The authors gratefully acknowledge the support provided by France's ANR ASTORIA under the research grant ANR-18-CE05-0015 and the Region of Normandy RIN Gaspropres project and Chile's National Agency for Research and Development (ANID) through research program Fondecyt/Regular 1191758. Also, this work was performed by the mobility France-Chile joint program receiving a research grant provided by Ecos/ANID C19E01.

Appendix A. Calibration of the scattered signal

Figure A.12 shows the radial profile of the acquired scattering signal before and after Abel deconvolution. The average level determined after deconvoltion $Ab^{-1}\left(P_{vv,C_2H_4}\right) = 0.0653$ is used to calibrate the scattering measurements.

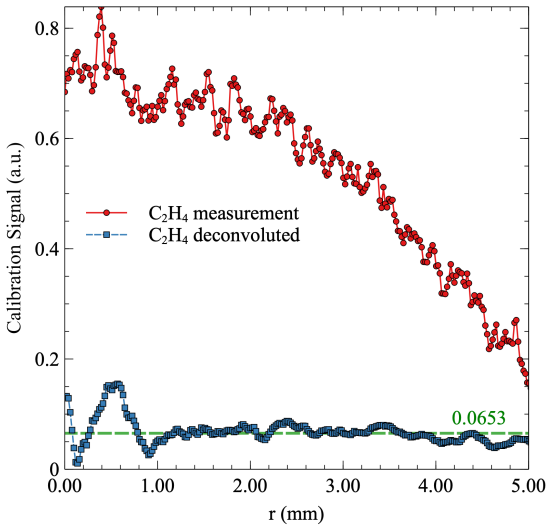

Figure A.12: The radial profiles of scattered signal obtained from a free jet of ethylene.

Appendix B. Analytical expression of gyration radius related moments

Equations B.1, B.2 and B.3 provide the analytical expressions of $\overline{R_g^{2D_f} f}$ for monodisperse, lognormal, and self-preserving aggregate size distributions, respectively

$$\overline{R_g^{2D_f} f} = R_g^{2D_f} f(qR_g) \tag{B.1}$$

$$\overline{R_g^{2D_f} f} = \int_0^\infty \frac{D_g^{2D_f-1} f(qR_g) e^{-\frac{1}{2}\left(\frac{ln(D_g/D_{geo})}{ln(\sigma_{geo})}\right)^2}}{2^{2D_f}\sqrt{2\pi} ln(\sigma_{geo})} dD_g \tag{B.2}$$

$$\overline{R_g^{2D_f} f} = \int_0^{\infty} \frac{D_f}{2^{2D_f}} \frac{(1-\lambda_{SP})^{(1-\lambda_{SP})}}{\Gamma(1-\lambda_{SP})} \frac{D_g^{D_f(3-\lambda_{SP})-2}}{\widetilde{D_g}^{D_f(1-\lambda_{SP})}} f(qR_g) e^{-(1-\lambda_{SP})\left(\frac{D_g}{\widetilde{D_g}}\right)^{D_f}} dD_g \tag{B.3}$$

Equations B.4, B.5 and B.6 are the analytical expressions of $\overline{R_g^{2D_f}}$ for monodisperse, Lognormal, and self-preserving aggregate size distributions, respectively

$$\overline{R_g^{2D_f}} = R_g^{2D_f} \tag{B.4}$$

$$\overline{R_g^{2D_f}} = \left(\frac{D_{geo}}{2}\right)^{2D_f} e^{2D_f^2 ln^2(\sigma_{geo})} \tag{B.5}$$

$$\overline{R_g^{2D_f}} = \left(\frac{\widetilde{D_g}}{2}\right)^{2D_f} \frac{2-\lambda_{SP}}{1-\lambda_{SP}} \tag{B.6}$$

Equations B.7, B.8 and B.9 provide the analytical expressions of $\overline{R_g^{D_f}}$ for monodisperse, lognormal, and self-preserving size distributions, respectively

$$\overline{R_g^{D_f}} = R_g^{D_f} \tag{B.7}$$

$$\overline{R_g^{D_f}} = \left(\frac{D_{geo}}{2}\right)^{D_f} e^{\frac{D_f^2 ln^2(\sigma_{geo})}{2}} \tag{B.8}$$

$$\overline{R_g^{D_f}} = \left(\frac{\widetilde{D_g}}{2}\right)^{D_f} \tag{B.9}$$

Appendix C. $F(m)$ and f_v based on multi-wavelength LOSA measurements

Figure C.13 shows the radial profiles of soot volume fraction at different HABs. These profiles were computed by considering the dependence of the scattering function $F(m)$ on the maturity coefficient β, as shown in Fig. C.14 (see [10] for details).

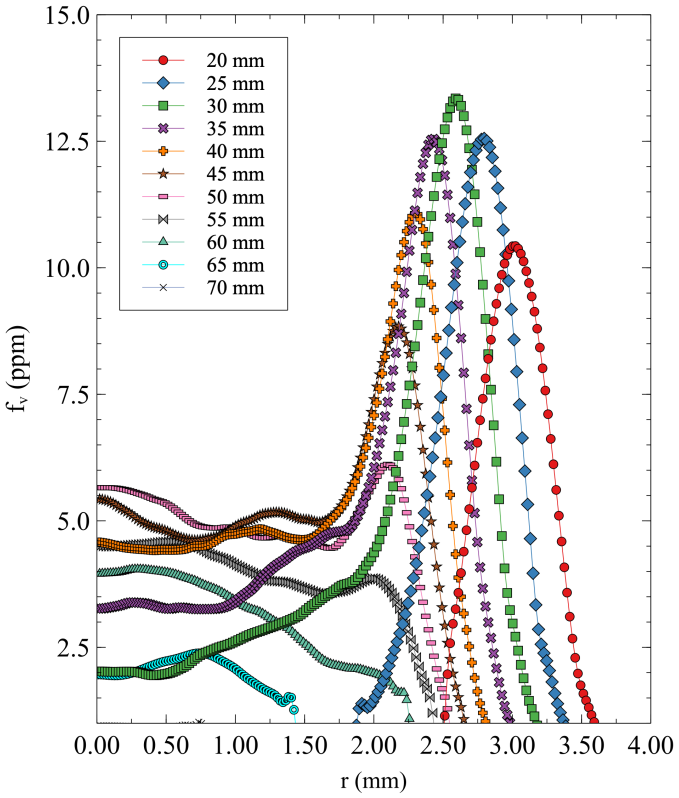

Figure C.13: Soot volume fraction as a function of the height above the burner (Data from [10])

Appendix D. CoFlame simulation of the ethylene diffusion flame

To complement the experiments and to provide useful details of the soot formation processes, the laminar coflow flame was simulated with the CoFlame code [50]. Details of the simulation are provided in [10]. The gas-phase kinetics is modeled with the DLR chemical mechanism [52]. The transport equations for the flow, species, energy, and soot are solved in a fully-coupled fashion. The population balance equations of soot aggregates and primary particles were solved using a sectional method considering soot nucleation due to collision of three five-ring polycyclic aromatic hydrocarbons (PAHs), surface growth via PAH adsorption (collision theory and sticking probability) of the same PAHs onto soot surface and by the

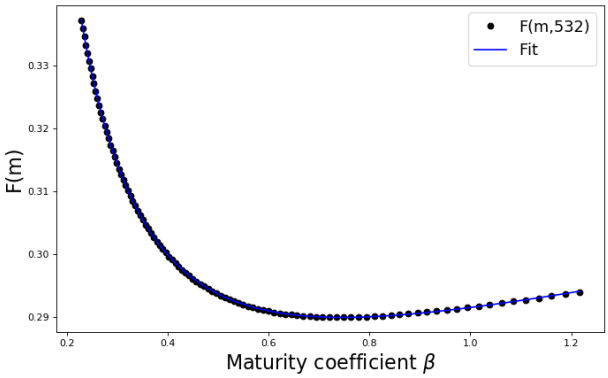

Figure C.14: Relationship between the maturity coefficient and the scattering function using the same methodology described in [10].

hydrogen-abstraction carbon-addition (HACA) mechanism [53], which includes surface oxidation by O_2 (HACA) and OH (collision theory), particle aggregation and oxidation-driven aggregate fragmentation. The rates of production/consumption by these processes are computed from the soot particle characteristics and related species concentrations (see [50] for details). Figure D.15 presents a qualitative description, from the converged solution of the flame simulation, of the different regions of the flame where nucleation, coagulation, PAH adsorption, HACA, OH and O_2 oxidation prevail.

Appendix E. Superiority of HPALS over conventional approaches

The main advantage of HPALS over conventional scattering techniques, such as 2D-MALS, is its ability to provide high spatial resolution over a wide range of scattering angle (except very small scattering angles in the forward direction or very large scattering angles in the backward direction), i.e., the spatial resolution of HPALS is independent of the scattering angle.

Indeed, in classical configuration of light scattering experiments (vertical laser light sheet or horizontal laser beam crossing the flame centerline, see Fig.E.16), the volume of measurement, which corresponds to the intersection between the laser and the signal collection optics, increases when scattering angle deviates from $\theta = \pi/2$. When the scattering signal is detected by a CCD camera, the spatial resolution of measurement, Δr, is related to a pixel on the camera with a width Δx, through $\Delta r = \Delta x / sin(\theta)$.

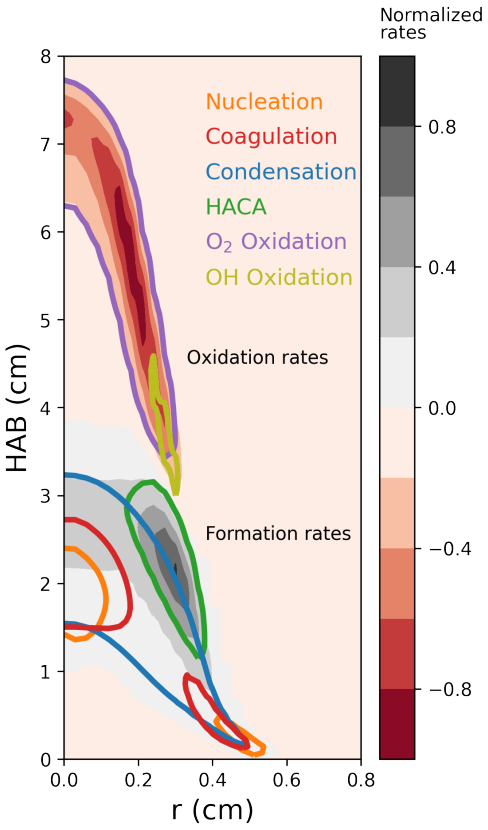

Figure D.15: Distributions of the different soot processes in the laminar ethylene diffusion flame based on the CoFlame simulation.

Therefore, even if the scattering intensity is corrected for the scattering-angle dependent measurement volume as in [34, 36], the detected scattering intensity is likely contributed from soot particles of different properties when the spatial resolution is poor at small and large scattering angles.

This tends to smooth the angle-resolved light scattering intensity, especially in the forward and backward directions. In consequence, the fitting process and the resulting radial distribution of aggregate size distribution parameters can be affected. This impact is evaluated in the present section. For this purpose, we consider the radial profile determined by HPALS since its spatial resolution is independent of scattering angle. To simulate the collected signals that would be measured by 2D-MALS after correction of

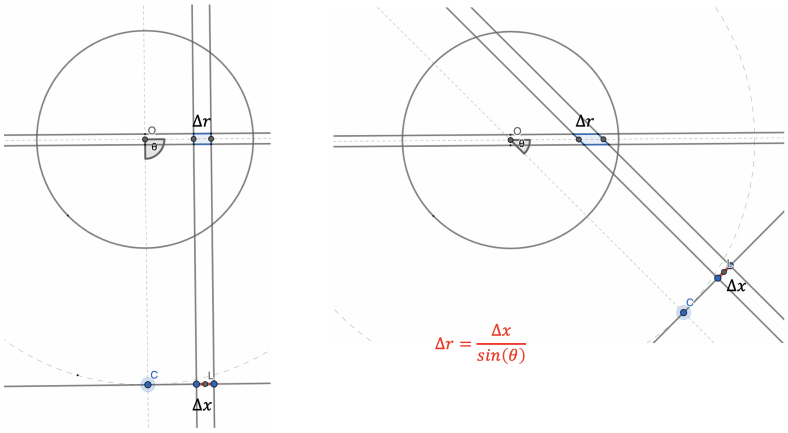

Figure E.16: Illustration of the change of measurement volume with changing the scattering angle in conventional vertical planar configuration (top view).

the intensity caused by angle-dependent measurement volume, the HPALS radial intensity profile is convoluted by a Gaussian function whose width is inversely proportional to $sin(\theta)$.

The convoluted signals are then processed using the same method as in the present experiments. The results are compared at two HABs of 30 mm and 40 mm, the later being the height where larger aggregates and stronger gradients have been detected (see Fig.E.17). It is clear from this figure that the reduced spatial resolution of 2D-MALS with varying scattering angle leads to lower aggregate size distribution parameters in the radial region of of strong gradients and of large aggregates around $r = 2.6$ mm at HAB $=$ 40 mm. The effect is much less pronounced in regions where the gyration diameter profile is relatively smooth at both HAB $= 40$ mm (outside the peak region between about $r = 2.5$ mm and 2.7 mm) and 30 mm. It is also interesting to notice that the simulated 2DMALS experiments artificially enlarges the sooting region slightly at both HAB $= 30$ and 40 mm, which is again caused by the reduced spatial resolution with varying scattering angles.

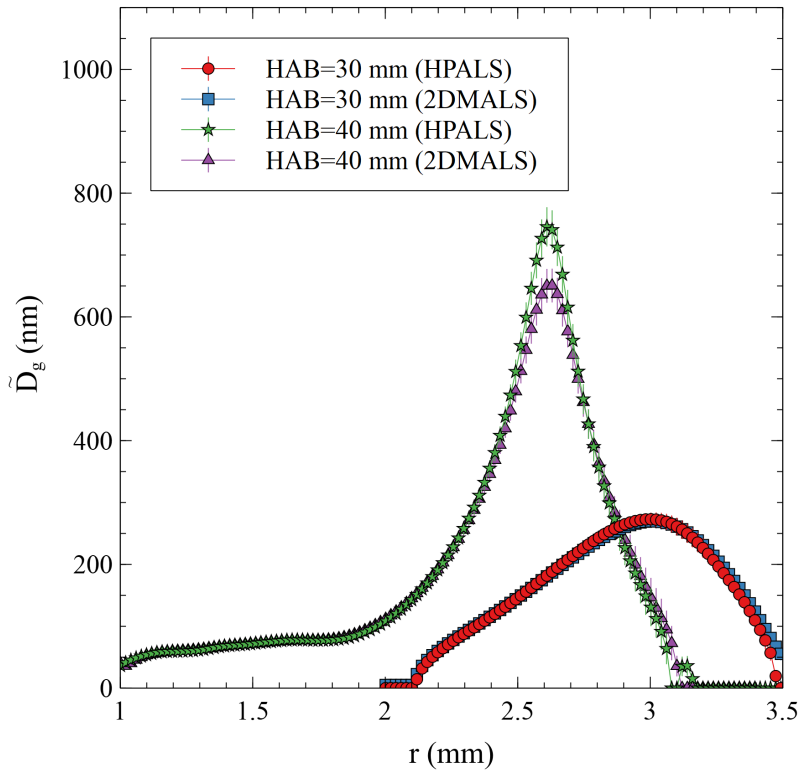

Figure E.17: Comparison of the gyration diameter governing parameter of the Self-Preserving size distribution obtained in the present study (HPALS) and as it should be measured with conventional vertical planar techniques as 2D-MALS. Comparison is performed at 2 HAB.

References

[1] H. Michelsen, C. Schulz, G. Smallwood, S. Will, Laser-induced incandescence: Particulate diagnostics for combustion, atmospheric, and industrial applications, Prog Energ Combust 51 (2015) 2–48.

[2] M. Bouvier, G. Cabot, J. Yon, F. Grisch, On the use of PIV, LII, PAH-PLIF and OH-PLIF for the study of soot formation and flame structure in a swirl stratified premixed ethylene/air flame, P Combust Inst (2020).

[3] C. Betrancourt, F. Liu, P. Desgroux, X. Mercier, A. Faccinetto, M. Salamanca, L. Ruwe, K. Kohse-Höinghaus, D. Emmrich, A. Beyer, et al., Investigation of the size of the incandescent incipient soot particles in premixed sooting and nucleation flames of n-butane using LII, HIM, and 1 nm-SMPS, Aerosol Sci Tech 51 (2017) 916–935.

[4] R. L. Vander Wal, T. M. Ticich, A. B. Stephens, Can soot primary particle size be determined using laser-induced incandescence?, Combust Flame 116 (1999) 291–296.

[5] F. J. Bauer, K. J. Daun, F. J. Huber, S. Will, Can soot primary particle size distributions be determined using laser-induced incandescence?, Appl Phys B-Lasers O 125 (2019) 1–15.

[6] E. Therssen, Y. Bouvier, C. Schoemaecker-Moreau, X. Mercier, P. Desgroux, M. Ziskind, C. Focsa, Determination of the ratio of soot refractive index function E(m) at the two wavelengths 532 and 1064 nm by laser induced incandescence, Appl Phys B-Lasers O 89 (2007) 417–427.

[7] G. Cléon, T. Amodeo, A. Faccinetto, P. Desgroux, Laser induced incandescence determination of the ratio of the soot absorption functions at 532 nm and 1064 nm in the nucleation zone of a low pressure premixed sooting flame., Appl Phys B-Lasers O 104 (2011).

[8] X. López-Yglesias, P. E. Schrader, H. A. Michelsen, Soot maturity and absorption cross sections, J Aerosol Sci 75 (2014) 43–64.

[9] J. Abboud, J. Schobing, G. Legros, A. Matynia, J. Bonnety, V. Tschamber, A. Brillard, G. Leyssens, P. Da Costa, Impacts of ester's carbon chain length and concentration on sooting propensities and soot oxidative reactivity: Application to Diesel and Biodiesel surrogates, Fuel 222 (2018) 586–598.

[10] J. Yon, J. J. Cruz Villanueva, F. Escudero, J. Morán, F. Liu, A. Fuentes, Revealing soot maturity based on multi-wavelength absorption/emission measurements in laminar axisymmetric coflow ethylene diffusion flames, Combust Flame 227 (2021) 147–161.

[11] L. Gallen, A. Felden, E. Riber, B. Cuenot, Lagrangian tracking of soot particles in LES of gas turbines, P Combust Inst 37 (2019) 5429–5436.

[12] A. Bouaniche, J. Yon, P. Domingo, L. Vervisch, Analysis of the soot particle size distribution in a laminar premixed flame: A hybrid stochastic/fixed-sectional approach, Flow Turbul Combust 104 (2020) 753–775.

[13] G. A. Kelesidis, S. E. Pratsinis, Estimating the internal and surface oxidation of soot agglomerates, Combust Flame 209 (2019) 493–499.

[14] J. Morán, A. Poux, J. Yon, Impact of the competition between aggregation and surface growth on the morphology of soot particles formed in an ethylene laminar premixed flame, J Aerosol Sci 152 (2020) 105690.

[15] M. M. Maricq, Coagulation dynamics of fractal-like soot aggregates, J Aerosol Sci 38 (2007) 141–156.

[16] C. Saggese, S. Ferrario, J. Camacho, A. Cuoci, A. Frassoldati, E. Ranzi, H. Wang, T. Faravelli, Kinetic modeling of particle size distribution of soot in a premixed burner-stabilized stagnation ethylene flame, Combust Flame 162 (2015) 3356–3369.

[17] C. Saggese, A. Cuoci, A. Frassoldati, S. Ferrario, J. Camacho, H. Wang, T. Faravelli, Probe effects in soot sampling from a burner-stabilized stagnation flame, Combust Flame 167 (2016) 184–197.

[18] M. Altenhoff, C. Teige, M. Storch, S. Will, Novel electric thermophoretic sampling device with highly repeatable characteristics, Rev Sci Instrum 87 (2016) 125108.

[19] R. Santoro, H. Semerjian, R. Dobbins, Soot particle measurements in diffusion flames, Combust Flame 51 (1983) 203–218.

[20] Ü. Ö. Köylü, G. M. Faeth, Radiative properties of flame-generated soot, J Heat Trans-T ASME 115 (1993).

[21] Ü. Ö. Köylü, G. M. Faeth, Optical Properties of Soot in Buoyant Laminar Diffusion Flames, J Heat Transf 116 (1994) 971–979.

[22] C. Sorensen, Light scattering by fractal aggregates: a review, Aerosol Sci Tech 35 (2001) 648–687.

[23] R. Puri, T. Richardson, R. Santoro, R. Dobbins, Aerosol dynamic processes of soot aggregates in a laminar ethene diffusion flame, Combust Flame 92 (1993) 320–333.

[24] S. Di Stasio, P. Massoli, M. Lazzaro, Retrieval of soot aggregate morphology from light scattering/extinction measurements in a high-pressure high-temperature environment, J Aerosol Sci 27 (1996) 897–913.

[25] Ü. Ö. Köylü, Quantitative analysis of in situ optical diagnostics for inferring particle/aggregate parameters in flames: implications for soot surface growth and total emissivity, Combust Flame 109 (1997) 488–500.

[26] G. Wang, C. M. Sorensen, Experimental test of the rayleigh-debye-gans theory for light scattering by fractal aggregates, Appl Optics 41 (2002) 4645–4651.

[27] R. K. Chakrabarty, H. Moosmüller, W. P. Arnott, M. A. Garro, J. G. Slowik, E. S. Cross, J.-H. Han, P. Davidovits, T. B. Onasch, D. R. Worsnop, Light scattering and absorption by fractal-like carbonaceous chain aggregates: Comparison of theories and experiment, Appl Optics 46 (2007) 6990–7006.

[28] J. Cai, N. Lu, C. Sorensen, Comparison of size and morphology of soot aggregates as determined by light scattering and electron microscope analysis, Langmuir 9 (1993) 2861–2867.

[29] S. De Iuliis, S. Maffi, F. Cignoli, G. Zizak, Three-angle scattering/extinction versus TEM measurements on soot in premixed ethylene/air flame, Appl Phys B-Lasers O 102 (2011) 891–903.

[30] C. Caumont-Prim, J. Yon, A. Coppalle, F.-X. Ouf, K. F. Ren, Measurement of aggregates' size distribution by angular light scattering, J Quant Spectrosc Ra 126 (2013) 140–149.

[31] H. Oltmann, J. Reimann, S. Will, Wide-angle light scattering (WALS) for soot aggregate characterization, Combust Flame 157 (2010) 516–522.

[32] M. Bouvier, J. Yon, G. Lefevre, F. Grisch, A novel approach for in-situ soot size distribution measurement based on spectrally resolved light scattering, J Quant Spectrosc Ra 225 (2019) 58–68.

[33] J.-Y. Zhang, H. Qi, Y.-F. Wang, B.-H. Gao, L.-M. Ruan, Retrieval of fractal dimension and size distribution of non-compact soot aggregates from relative intensities of multi-wavelength angular-resolved light scattering, Opt Express 27 (2019) 1613–1631.

[34] B. Ma, M. B. Long, Combined soot optical characterization using 2-d multi-angle light scattering and spectrally resolved line-of-sight attenuation and its implication on soot color-ratio pyrometry, Appl Phys B-Lasers O 1 (2014) 287–303.

[35] N. J. Kempema, M. B. Long, Combined optical and tem investigations for a detailed characterization of soot aggregate properties in a laminar coflow diffusion flame, Combust Flame 164 (2016) 373–385.

[36] M. Altenhoff, S. Aßmann, J. F. Perlitz, F. J. Huber, S. Will, Soot aggregate sizing in an extended premixed flame by high-resolution two-dimensional multi-angle light scattering (2D-MALS), Appl Phys B-Lasers O 125 (2019) 176.

[37] P. Kheirkhah, A. Baldelli, P. Kirchen, S. Rogak, Development and validation of a multi-angle light scattering method for fast engine soot mass and size measurements, Aerosol Sci Tech (2020) 1–19.

[38] H. M. Amin, W. L. Roberts, Soot measurements by two angle scattering and extinction in an N2-diluted ethylene/air counterflow diffusion flame from 2 to 5 atm, P Combust Inst 36 (2017) 861–869.

[39] C. M. Sorensen, J. Yon, F. Liu, J. Maughan, W. R. Heinson, M. J. Berg, Light scattering and absorption by fractal aggregates including soot, J Quant Spectrosc Ra 217 (2018) 459–473.

[40] J. Yon, F. Liu, A. Bescond, C. Caumont-Prim, C. Rozé, F.-X. Ouf, A. Coppalle, Effects of multiple scattering on radiative properties of soot fractal aggregates, J Quant Spectrosc Ra 133 (2014) 374–381.

[41] S. T. Moghaddam, P. J. Hadwin, K. J. Daun, Soot aggregate sizing through multiangle elastic light scattering: Influence of model error, J Aerosol Sci 111 (2017) 36–50.

[42] S. Talebi-Moghaddam, F. Bauer, F. Huber, S. Will, K. Daun, Inferring soot morphology through multi-angle light scattering using an artificial neural network, J Quant Spectrosc Ra (2020) 106957.

[43] H. Michelsen, Probing soot formation, chemical and physical evolution, and oxidation: A review of in situ diagnostic techniques and needs, P Combust Inst 36 (2017) 717–735.

[44] J. Yon, F.-X. Ouf, D. Hebert, J. B. Mitchell, N. Teuscher, J.-L. Le Garrec, A. Bescond, W. Baumann, D. Ourdani, T. Bizien, et al., Investigation of soot oxidation by coupling LII, SAXS and scattering measurements, Combust Flame 190 (2018) 441–453.

[45] D. D. Hickstein, S. T. Gibson, R. Yurchak, D. D. Das, M. Ryazanov, A direct comparison of high-speed methods for the numerical abel transform, Rev Sci Instrum 90 (2019) 065115.

[46] D. Cortés, J. Morán, F. Liu, F. Escudero, J.-L. Consalvi, A. Fuentes, Effect of fuels and oxygen indices on the morphology of soot generated in laminar coflow diffusion flames, Energ Fuel 32 (2018) 11802–11813.

[47] R. A. Dobbins, C. M. Megaridis, Absorption and scattering of light by polydisperse aggregates, Appl Optics 30 (1991) 4747–4754.

[48] J. Morán, J. Yon, A. Poux, F. Corbin, F.-X. Ouf, A. Siméon, Monte carlo aggregation code (MCAC) part 2: Application to soot agglomeration, highlighting the importance of primary particles, J Colloid Interf Sci 575 (2020) 274–285.

[49] M. L. Botero, N. Eaves, J. A. Dreyer, Y. Sheng, J. Akroyd, W. Yang, M. Kraft, Experimental and numerical study of the evolution of soot primary particles in a diffusion flame, P Combust Inst 37 (2019) 2047–2055.

[50] N. A. Eaves, Q. Zhang, F. Liu, H. Guo, S. B. Dworkin, M. J. Thomson, Coflame: A refined and validated numerical algorithm for modeling sooting laminar coflow diffusion flames, Comput Phys Commun 207 (2016) 464–477.

[51] R. Santoro, T. Yeh, J. Horvath, H. Semerjian, The transport and growth of soot particles in laminar diffusion flames, Combust Sci Technol 53 (1987) 89–115.

[52] S. B. Dworkin, Q. Zhang, M. J. Thomson, N. A. Slavinskaya, U. Riedel, Application of an enhanced pah growth model to soot formation in a laminar coflow ethylene/air diffusion flame, Combust Flame 158 (2011) 1682–1695.

[53] J. Appel, H. Bockhorn, M. Frenklach, Kinetic modeling of soot formation with detailed chemistry and physics: laminar premixed flames of C2 hydrocarbons, Combust Flame 121 (2000) 122–136.